Connected-Element Interferometer Holography with Polar Sampling

Alberto Torre* and Manuel Vazquez*

ABSTRACT. — Connected-element interferometer (CEI) holography is a technique that enables holography on DSN antennas at the operational frequency bands. If one DSN antenna is tracking a spacecraft with a powerful enough signal, it could be used as the reference for an antenna whose surface has to be measured. This opportunistic scheme is hampered by the impact of tropospheric turbulence in the resulting holographic map. With Cartesian grid holography, this means that measurements can only be done at night, when the troposphere is mostly calm. That reduces the chances in which CEI holography can be done. In the present report, a polar grid is used to reduce the impact of the troposphere. In this way, CEI holography can be done at any time an antenna is available, regardless of the status of the troposphere. Simulations and actual measurements done using polar sampling are presented and compared with Cartesian sampled maps.

I. Introduction

Connected-element interferometry is based on correlating the signal received by two DSN antennas to get the relative phase and amplitude between them [1]. As mentioned in Section II.b of [1], the impact of tropospheric phase noise in the final holography maps is severe. CEI holography could only be used during clear troposphere conditions, such as winter nights. The main idea behind the development of CEI holography is twofold: Firstly, having a tool to map the dish at operational bands, and secondly, having a tool that can be used at anytime to take advantage of free times in the antenna schedule. To fulfill the second criteria, a technique to reduce the impact of the troposphere in the phase measurements should be used. One possible solution could be the installation of water vapor radiometers to calibrate the troposphere at each antenna. This solution would be costly and difficult to implement.

---

*Madrid Deep Space Communications Complex

The research described in this publication was carried out by the Jet Propulsion Laboratory, California Institute of Technology, under a contract with the National Aeronautics and Space Administration.

Another solution, which will be described in this report, is to use a polar sampling scheme of the far field during the holography data acquisition.

Microwave holography is based on taking samples of the Fourier transform of the aperture field, for later inverse transformation. There are many other inverse problems in which one can consider the available data to be samples of the Fourier transform of a function, and the goal is the reconstruction of this function from the noisy samples of its Fourier transfom. Examples include magnetic resonance imaging, aperture synthesis, and computer-aided tomography [2].

Traditionally, samples are taken on a Cartesian grid, which is very convenient for later processing with a fast Fourier transform (FFT). However, if the object to be imaged is moving, ghosting artifacts appear during the inverse transformation. Under these conditions, polar sampling is used due to its decreased motion sensitivity and the overall reduction in aliasing artifacts [3]. Another advantage of the polar sampling scheme is the fact that the center of the sampling space is oversampled and continuously updated due to overlapping spokes that repeatedly pass through the center. When taking samples from the far field of an antenna, the boresight region (mainlobe and first sidelobes) concentrates most of the energy. Therefore, oversampling this region yields an averaging effect and will contribute to having a better image of the main large-scale features of the aperture function. For instance, subreflector displacements and tilts reflect themselves in asymmetries in the first sidelobes. With a polar sampling scheme, these first sidelobes are scanned multiple times at different but close points, providing a certain degree of redundant information such that a failure in taking any of these points does not affect the overall estimated subreflector parameters so much. Besides, since the exact center of the far field is sampled at every spoke, wandering phase and amplitude deviations can be compensated more often. Regular Cartesian grid holography requires "beampeaks" to be executed every five scans to sample the far field center. With polar sampling, this is done at every single scan without losing time.

Polar sampling has several disadvantages. The main one is the increased processing complexity. To start with, there is no closed unique solution to reconstruct the image from the polar grid samples. Many techniques have been proposed and are being used [2], with gridding being the most popular. The next section will address how to process polar sampled data.

II. Polar Sampling

As mentioned previously, there is evidence in the scientific literature that a polar sampling scheme reduces motion artifacts [4]. The far field of a large reflector antenna can be expressed as [5]:

$$T(u,v) = e^{j2kF} \int_S |J(x,y)| \, e^{-j\delta} e^{-jk(ux+vy)} dxdy \tag{1}$$

The holography data processing estimates the aperture function by computing the inverse Fourier transform of the far field:

$$Q(x,y) = |J(x,y)| \, e^{j2kF} e^{-j\delta} = \mathcal{F}^{-1}[T(u,v)] \tag{2}$$

When the far field is acquired with a Cartesian grid $\Delta u = \Delta v = \frac{\kappa}{D/\lambda}$ with κ being the inverse of the oversampling factor (typically $\kappa = 0.85$) and D the antenna diameter, then the usual two-dimensional discrete Fourier transform (2D-DFT) is obtained:

$$T(p\Delta u, q\Delta v) = s_x s_y \sum_{n=-N/2}^{N/2-1} \sum_{m=-N/2}^{N/2-1} Q(ns_x, ms_y) \exp\left(-j2\pi\left(\frac{np}{N} + \frac{mq}{N}\right)\right) \tag{3}$$

This expression has infinite support in the angular domain, and extends to $\pm\infty$. Nevertheless, if the data are properly sampled, the aperture illumination can be obtained through a simple inverse Fourier transform:

$$Q(ns_x, ms_y) = \frac{1}{s_x s_y} \sum_{p=-P/2}^{P/2-1} \sum_{q=-P/2}^{P/2-1} T(p\Delta u, q\Delta v) \exp\left(j2\pi\left(\frac{np}{N} + \frac{mq}{N}\right)\right) \tag{4}$$

Truncation of the far field data causes Gibbs ringing near sharp discontinuities that can be minimized by apodization of the data. Apart from that, the aperture function can be readily obtained from equation (4); iterative algorithms to improve the final image such as the one in [5] can be used. If polar sampling is used, the far field that is sampled at u, v points can be described by:

$$\rho = (p\Delta\rho)\cos(q\Delta\phi) \tag{5}$$

$$\phi = (p\Delta\rho)\sin(q\Delta\phi) \tag{6}$$

so the far field is

$$\begin{aligned} T_{polar}(r\Delta\rho, s\Delta\phi) = T_{polar}(\rho,\phi) = T((r\Delta\rho)\cos(s\Delta\phi), (r\Delta\rho)\sin(s\Delta\phi)) = \\ = e^{j2kF} \int_S Q(x,y) \, e^{-jk(r\Delta\rho\cos(s\Delta\phi)x + r\Delta\rho\sin(s\Delta\phi)y)} dxdy \end{aligned} \tag{7}$$

The first thing to establish in equation (7) is the sampling requirements in the radial and angular components. When sampling in the radial component, the resulting point

spread function can be decomposed into a main lobe whose behavior is jinc-like ($J_1(r)/r$), and a series of assymmetric ring lobes at $j/\Delta k_r$ whose peak amplitude decay as j (ring order) increases [6]. The replicates are located at multiples of $1/\Delta k_r$ as in Cartesian sampling ($1/\Delta k_x$,$1/\Delta k_y$), but in polar sampling are not exact duplicates of the main lobe but differ both in shape and amplitude. Moreover, in Cartesian sampling, complex exponentials lead to coherent summation, but in contrast, in polar sampling Bessel functions' non-purely periodic nature leads to asymmetric polar ring lobes of decreasing amplitude. Besides, these oscillations have non-equidistant zero-crossings in the radial direction, that produce a radial ringing (or truncation) artifact and signal leakage. This means that even if the Nyquist criterion is met ($\Delta k_r < D/\lambda$), the ring lobes will introduce some aliasing, since the convolution of the object with the ring lobes will distribute ring lobe energy into the effective field of view. Aliasing will contribute to increasing the level of distortion in the aperture illumination; it is shown by [6], that the signal-to-noise ratio (SNR) of the polar sampling is a factor of $2/\sqrt{3}$ lower than the Cartersian one (0.6 dB loss).

Ring lobes amplitude relative to the main lobe is given by [6]:

$$\frac{|s_j|}{|s_0|} \approx \frac{2.25}{\pi\sqrt{\pi K j}} \tag{8}$$

where $2K+1=N$ is the holography grid number of points. This means that the larger the extent of the far field is acquired, the less aliasing and Gibbs effect will appear in the aperture field domain.

Regarding the effects of sampling in the angular domain, the point response is again seen as a superposition of Bessel functions of different orders [7]. The number of spokes (N_a) from 0 to π required to prevent aliasing inside the antenna aperture is [7]:

$$N_a > \pi R r_{max} = \pi D/\lambda \frac{\kappa}{D/\lambda} N_r = \pi\kappa N_r \approx 2.5 N_r \tag{9}$$

For implementation purposes, a value of $3N_r$ is chosen. Figure 1a shows a 11×11 grid and an equivalent polar grid with only 10 angular spokes from 0 to π. If this polar grid were used, the resolution would be lower as the corners of the Cartesian grid are not covered. To avoid this problem, the polar grid is increased radially by a factor of $\sqrt{2}$. The resulting grid is shown in figure 1b. This new grid has a lower point density. To avoid aliasing artifacts, the number of radial points is increased by 3 in practice. This does not suppose any penalty in the acquisition time, as the antenna moves radially, so in practice all radial points are available; the only penalty comes from the fact that the radial extension is $\sqrt{2}$ longer. All polar holographies shown in this report are done with this scheme; the radial extension is increased by a factor of $\sqrt{2}$ and three more points are acquired radially (a 127 radial points x 127 angles polar grid has 381 points in each spoke). On the other hand, increasing by three in the angular

dimension would triple the acquisition time. The next section shows a interpolation technique to avoid this problem.

A. Computing the Inverse Fourier Transform of Polar Sampled Data

Equation (7) does not have a closed equivalent equation for computing the aperture field, as in the case of the Cartesian grid (see equation (4)). The first approach to compute the aperture field is to regrid the polar sampled data to a rectangular grid and then compute the aperture field through equation (4). In gridding algorithms, the idea is to pass a convolution kernel $W(u,v)$ over the data sampled on the polar grid, with the convolution output evaluated at the points of the Cartesian grid. In polar coordinates, this convolution step is

$$T^c_{polar}(\rho,\phi) = T_{polar}(\rho,\phi) * W(\rho,\phi) = \\ = \int_0^{2\pi}\int_0^{\infty} T_{polar}(\xi,\varphi)\, W(\rho-\xi\cos\varphi, \rho-\xi\sin\varphi)\, \xi d\xi d\varphi \quad (10)$$

The contribution of the kernel is then removed by division by $w(x,y)$ after the 2D inverse FFT. If the sinc and Dirichlet kernels are used for the ρ and ϕ variables, then [8]:

$$T(p\Delta u, q\Delta v) = \sum_{r=0}^{\infty}\sum_{k=0}^{N-1} T_{polar}(r\Delta\rho, s\Delta\phi)\,\mathrm{sinc}\left(\Delta\rho\left(p\Delta u - \frac{r}{\Delta\rho}\right)\right)\sigma\left(q\Delta v - \frac{2\pi k}{N}\right) \quad (11)$$

where σ is the Dirichlet kernel

$$\sigma(\phi, N) = \frac{\sin\left(\frac{1}{2}(N-1)\phi\right)}{N\sin\left(\frac{1}{2}\phi\right)} \quad (12)$$

The regridding in equation (11) works as long as two conditions are met. First, as in the case of the Cartesian grid, the far field must be completely sampled $\rho = \infty$. Second, the Fourier transform in polar coordinates should be band-limited to L and $N > 2L+1$. None of these conditions were met for equation (11).

There are other algorithms that work by computing the inverse Fourier transform on a Cartesian grid from the polar samples of the Fourier transform. No regridding algorithms are required. The nonuniform FFT or the pseudopolar FFT are some examples. The algorithm used in [9] offers an exact solution for the direct polar Fourier transform, with no assumptions made on the sampled function. For the inverse polar FFT, there is no exact solution; instead a generalized pseudo-inverse is

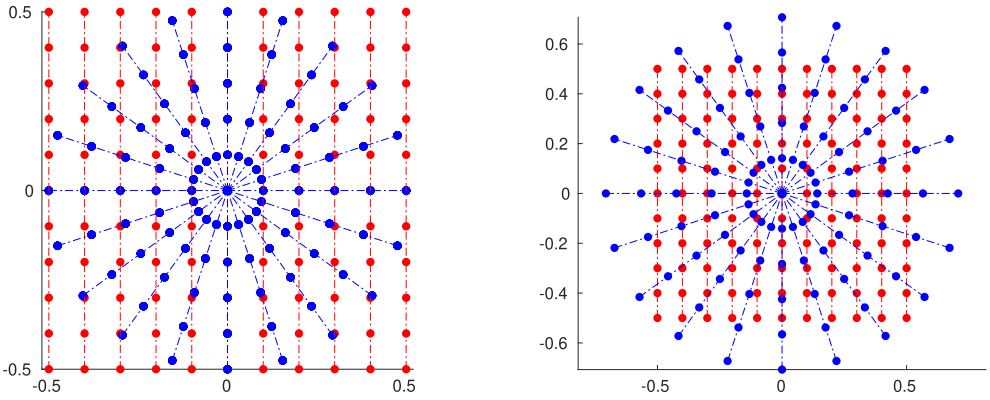

(a) Original grid **(b) Extended polar grid**

Figure 1. Cartesian and polar u-v grids.

calculated by means of an iterative gradient conjugate algorithm. This algorithm exhibits good accuracy and convergence, and it was selected for this report; its code can be found in [10]. The only drawback is the execution time, around 3 minutes for mid-resolution holography with 50 iterations.

In order to check the accuracy of the polar sampling method, a physical optics simulator of the antenna dish has been developed. This simulator takes into consideration the dual-shaped geometry of the 34-meter DSN antennas, the feed function, and the blockage due to the struts and subreflector. After computing the far field in the points determined by the sampling scheme, a corresponding holography is made. Figure 2a shows the result for a high-resolution holography of a 34-meter antenna with a perfect surface with polar sampling and no other system errors (tropospheric or thermal noise). As the dish has zero errors on its surface, the holography shows the residual effect on the map of the feed function, plus the border effects and the errors due to the sampling scheme. The same holography has been done with a Cartersian grid (see Figure 2b). Both images are quite similar; the Cartesian one shows more border effects close to the border of dish, while the polar one shows more border effects close to the struts. The deviations from the perfect surface are in the order of ± 0.1 mm at its peak, which is approximately 1/360 of the wavelength (1 degree in phase). Increasing the accuracy is mainly achieavable by moving to higher frequency bands. Other techniques can be used to slightly improve the accuracy, such as apodization of the acquisition window to decrease border effects, or characterization of the feed function for later removal.

Regarding resolution, the two previous holographies are repeated with three patches of 0.75×0.75 square meters raised (holography resolution is 0.33 meters). As seen in Figure 3a, the polar holography loses resolution in comparison with the Cartesian one shown in 3b.

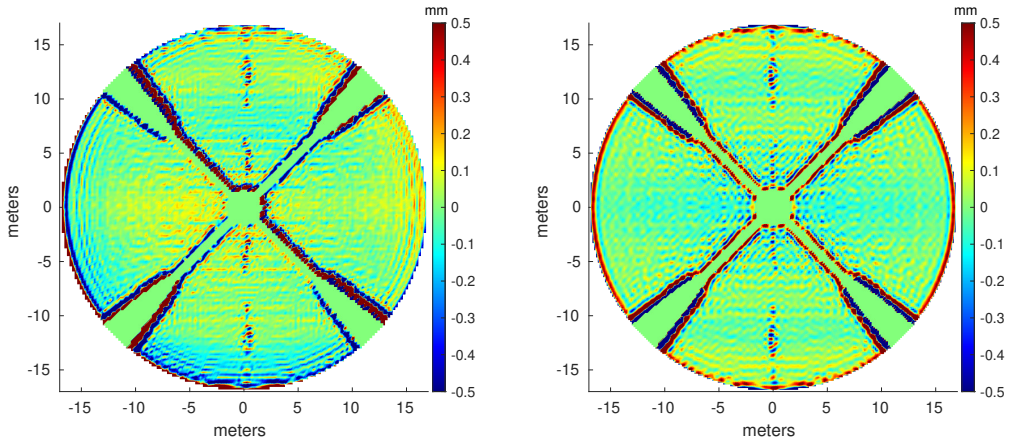

(a) 127 radial points x 127 angles (b) Cartesian 127x127

Figure 2. Simulated holographies of a 34-meter antenna without surface errors.

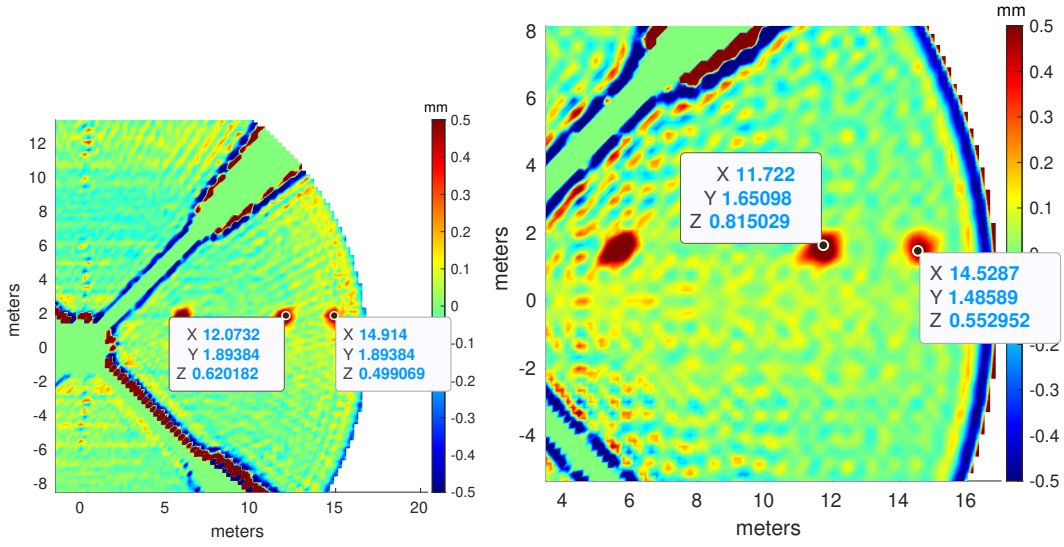

(a) 127 radial points x 127 angles (b) Cartesian 127x127

Figure 3. Simulated holographies of a 34-meter antenna with 3 panels raised.

One way to increase the resolution of the polar holography is by increasing its extension, as it has been shown in previous section. Radially it can be easily solved by increasing the extension by a factor of $\sqrt{2}$. Angularly, it would require more spokes. Those additional spokes can be obtained by interpolation with the Dirichlet kernel (Equation (12)). In the central regions of the grid, where the beam pattern is heavily oversampled, the interpolation is done without error. In the outer regions, some error is introduced. The grid for an hypothetical 11-point holography is shown in Figure 4. Blue dots represent the sampled data; green dots are the interpolated data with the Dirichlet kernel.

The resulting dish image using this interpolation technique is shown in Figure 5a; the resolution now is even better than in the Cartesian holography. This increased resolution comes with a price; the border effect close to the struts is higher (this ripple is where, presumably, the energy of the interpolation error from the outer parts of the far field goes to). This effect has been observed in actual holography; ripples appear close to the struts when angular interpolation is used. However, not doing this angular intepolation means losing resolution, and the resulting dish image is blurred.

All of these errors are reduced when increasing the frequency from X-band to Ka-band due to the increased accuracy. The result of doing the same holography in Ka-band is shown in Figure 6a. The ripples emanating from the struts are greatly reduced, and the patches are clearly seen as rectangular objects. The true height of the panels is also shown (Figure 5b). In order to see the remaining error, the scale must be reduced (Figure 6b).

B. Tropospheric Noise

Now, let's check the behavior of a Cartesian CEI holography under the effects of tropospheric noise. Under these circumstances, the phase measurement is corrupted by atmospheric turbulence, which can be modeled as shown in [11]. This turbulence has a certain degree of spatial and temporal correlation, which manifests in the error map as hot spots, instead of a uniform background noise as in the case of thermal noise. Besides, these hot spots appear in the image in different positions every time a new holography is done (see Simulation 1 in Figure 7a vs Simulation 2 in Figure 7b). As a consequence of this, Cartesian holographies can only be done under quiet troposphere conditions.

If the holographies are done with a polar sampling scheme, the results in Figures 8a and 8b are obtained. Hot spots are greatly reduced, and more importantly, the resulting maps are nearly identical. This assures repeatability of the measurements.

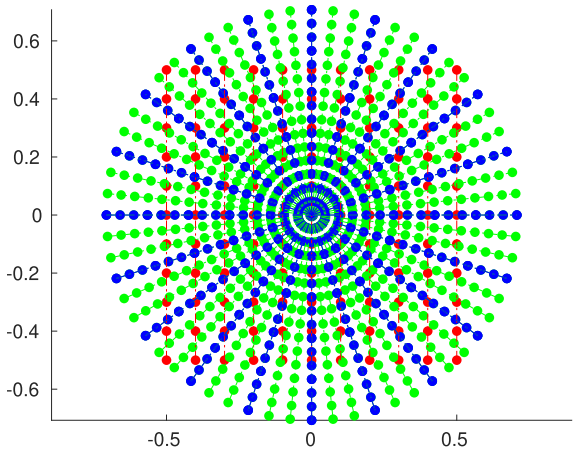

Figure 4. Cartesian (11x11) vs increased extent polar (11x10) u-v grid.

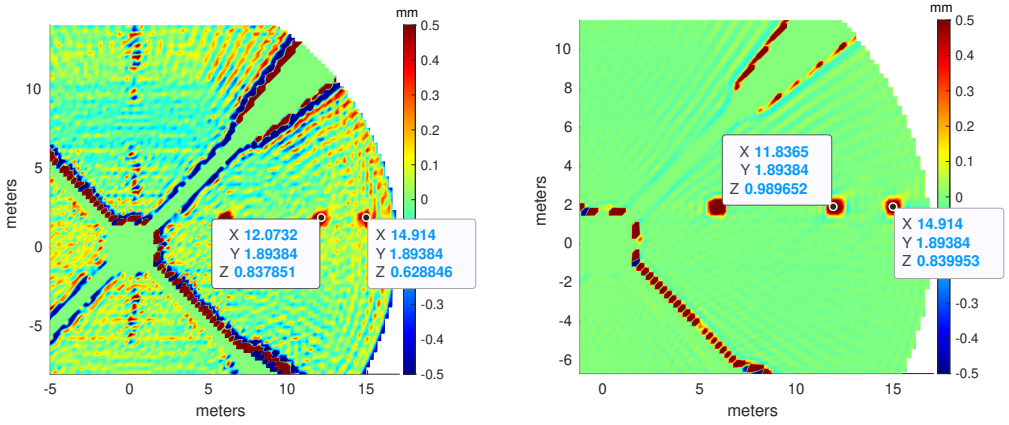

(a) X-band polar 127 x 127

(b) Ka-band polar 127 x 127

Figure 5. Simulated holography of a 34-meter antenna with 3 panels raised with interpolation=3.

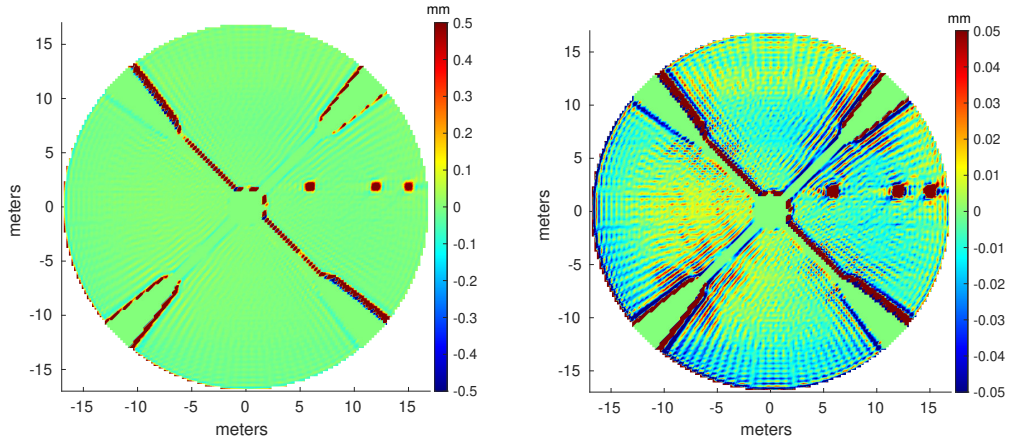

(a) Original scale (b) Reduced scale

Figure 6. Simulated polar holography of a 34-meter antenna in Ka-band with 3 panels raised with interpolation=3.

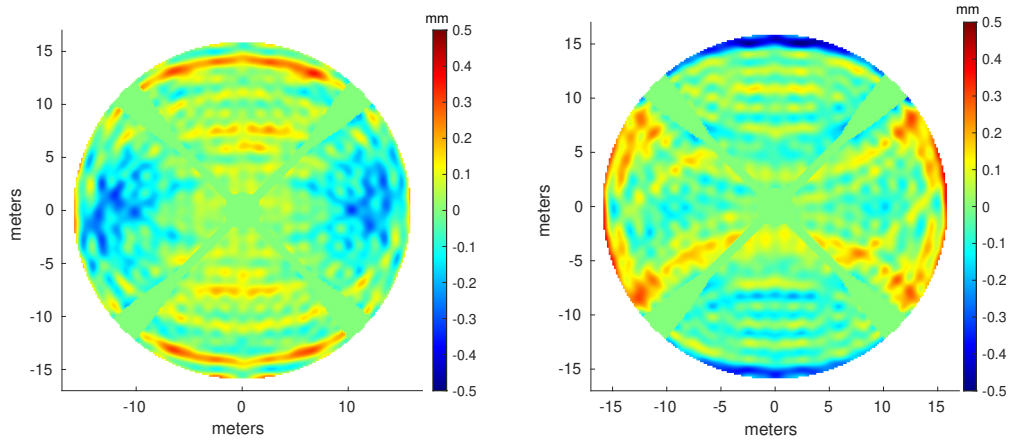

(a) Simulation 1 (b) Simulation 2

Figure 7. 51 x 51 Cartesian X-band holography of a 34-meter antenna under tropospheric noise with $\sigma = 17$ degrees.

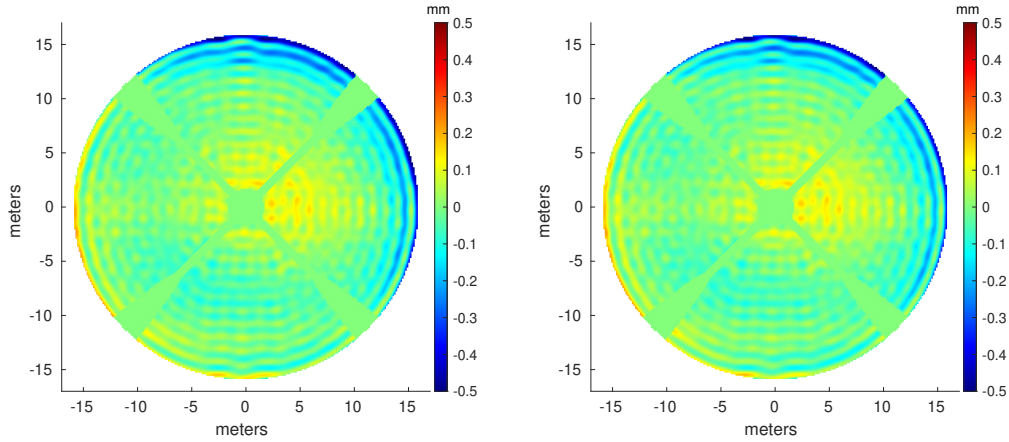

(a) Simulation 1 (b) Simulation 2

Figure 8. 51 x 51 polar X-band holography of a 34-meter antenna under tropospheric noise with $\sigma = 17$ degrees.

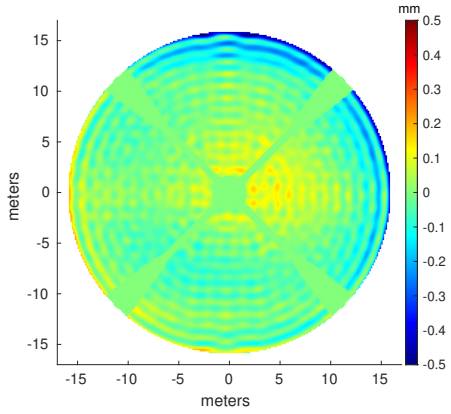

Figure 9. 51 x 51 polar X-band holography of a 34-meter antenna without tropospheric noise.

III. Measurements

During September 2023, a holography campaign was carried out at Madrid Deep Space Communication Complex (MDSCC) with the aim of assesing the status of DSS-63. Some polar holographies were done and compared with the Cartesian ones. On day of year (DOY) 263 and 264, high-resolution holographies were done in Ku-band with a beacon from Intelsat 37E at 11.199 GHz and 41.1 degrees of elevation. The phase maps (Figure 11) are practically the same in both cases, polar and Cartesian. The root mean square (rms) error was 1.15 mm for the Cartesian holography and 1.23 mm for the polar one. A later holography done on DOY 268 reported 1.22 mm for the polar holography and 1.24 for the Cartesian one. Interpolation effects are hardly noticeable in the polar holography; some ripples appear only in areas close to the struts. All main features of Cartesian holography appear in the polar one.

When we take a look at the amplitude maps (Figure 10), it is worth noting that the Cartesian holography has green areas due to the tropospheric noise. On the contrary, the polar holography shows a smooth amplitude map.

The effect of tropospheric turbulences can be better observed when CEI holographies are done during daytime, specially in summer time. On DOY 171, 2023, two holographies were done consecutively on DSS-53, one polar (time 12:32, average elevation=43 degrees) and the other Cartesian (time 14:02, average elevation=30 degrees), close to noon. The radio source was 3C84 and the reference antenna DSS-55. The heavy turbulence renders the Cartesian holography useless. The amplitude map (Figure 12a) has zones where the amplitude is lost, and the phase map (Figure 13a) shows large hot spots that are due to the accumulation of noise. On the contrary, the amplitude map in the polar holography is smooth (Figure 12b). The phase map in the polar holographies does not show large error areas (Figure 13b). For comparison purposes, the high-resolution Ku-band map (41 degrees of elevation) of the dish is shown in Figure 14a. The red zone at the bottom of Figure 13b is due to gravity distortion as the dish in polar holography is below the rigging angle. Figure 14b shows another polar CEI holography, this time closer to the rigging angle. The resemblance to the high-res Ku-band holography is higher.

One last set of measurements that shows the advantages of CEI and polar techniques working together is shown in Figure 15. On the left, a Ku-band high-resolution holography done on DOY 299, 2022, is shown. On the right, a K-band holography done on DOY 024, 2024, with the James Webb Space Telescope (JWST) spacecraft and DSS-54 as reference is shown. DSS-54 was tracking JWST as part of its regular operation schedule. As JWST has a powerful signal, the holography was done in less than 40 minutes as compared to the five hours required by a Ku-band holography. Rms error was lower in the case of the K-band holography due to poorer resolution (75 versus 127 grid). Nevertheless, the map is nearly identical to the one taken two years ago with the legacy Ku-band holography system.

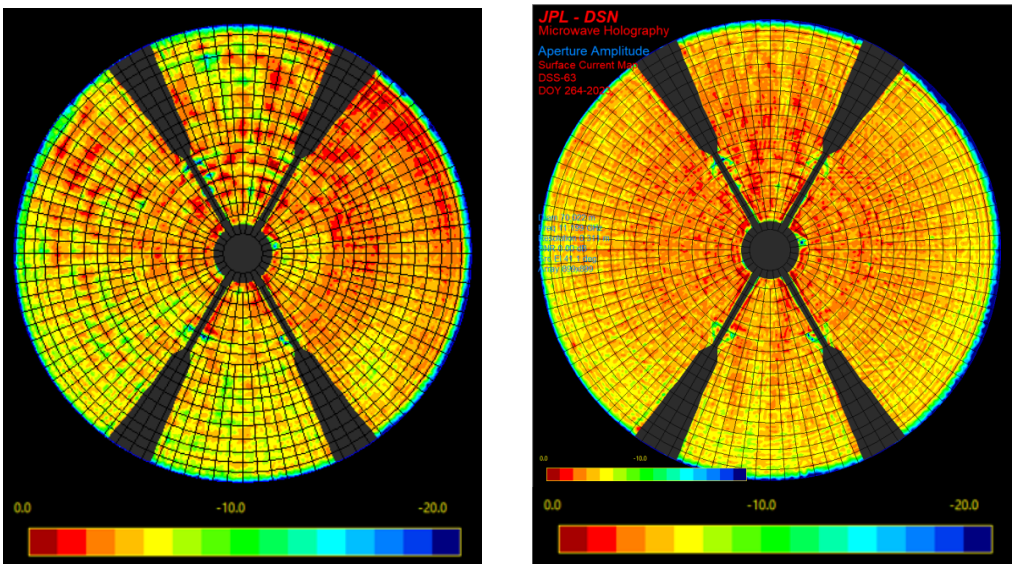

(a) Cartesian 197 x 197

(b) Polar 197 radius x 197 angles interpolated by 3

Figure 10. DSS-63 Ku-band high-resolution holographies (amplitude).

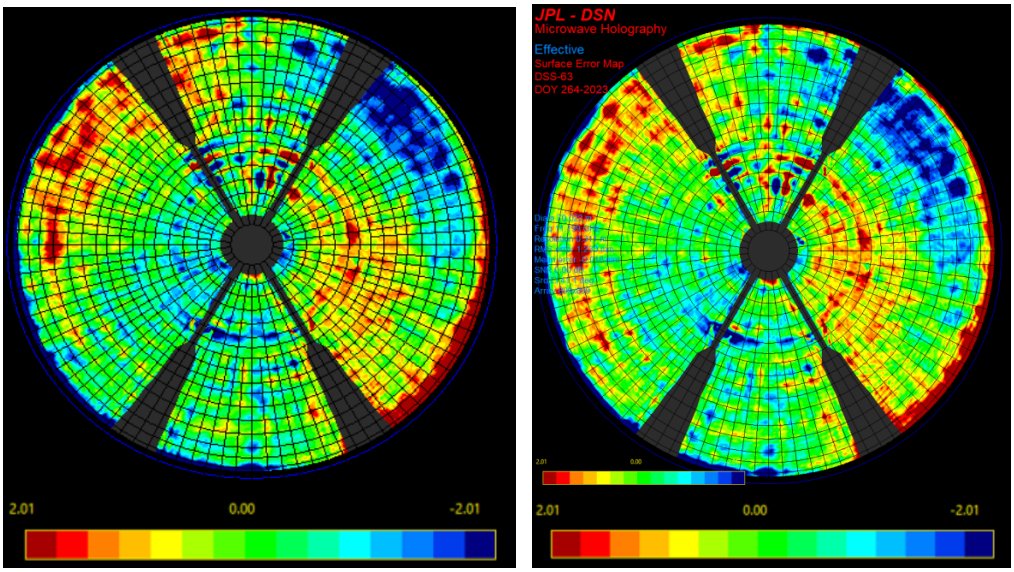

(a) Cartesian 197 x 197

(b) Polar 197 radius x 197 angles interpolated by 3

Figure 11. DSS-63 Ku-band high-resolution holographies (phase).

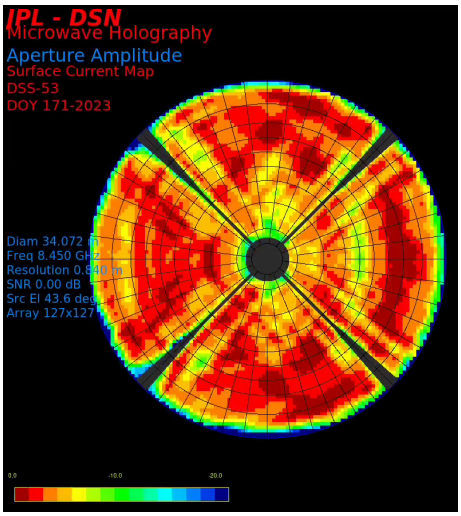

(a) Cartesian 51 x 51

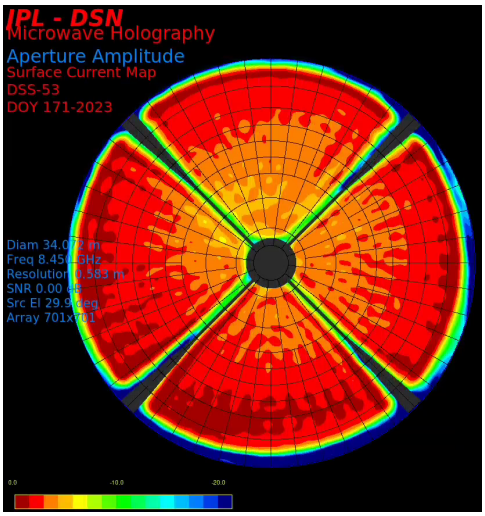

(b) Polar 51 radius x 51 angles interpolated by 3

Figure 12. DSS-53 X-band mid-resolution holographies (amplitude).

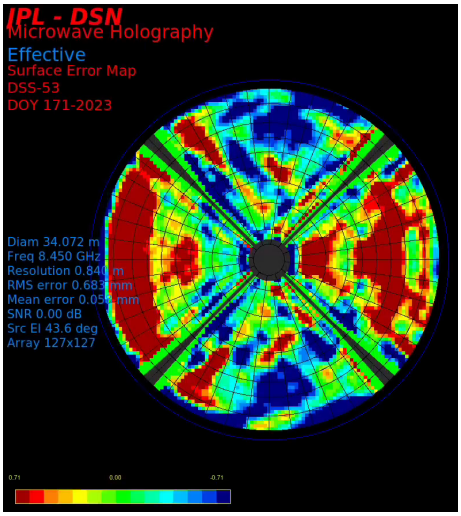

(a) Cartesian 51 x 51

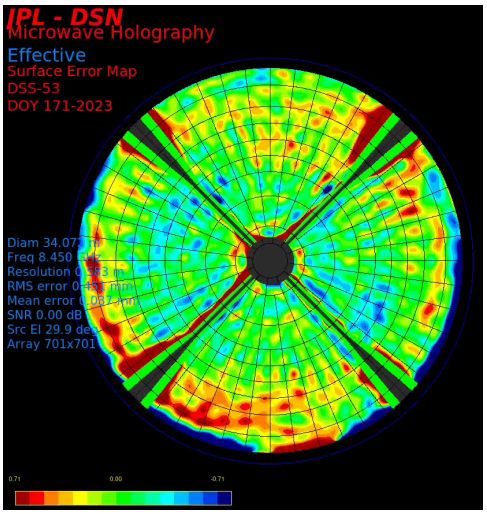

(b) Polar 51 radius x 51 angles interpolated by 3

Figure 13. DSS-53 X-band mid-resolution holographies (phase).

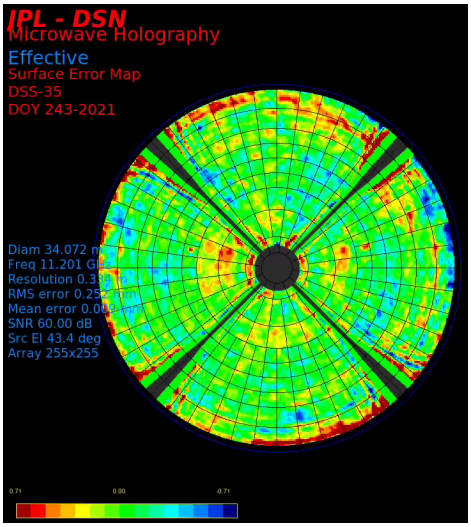

(a) 127 x 127 Ku-band

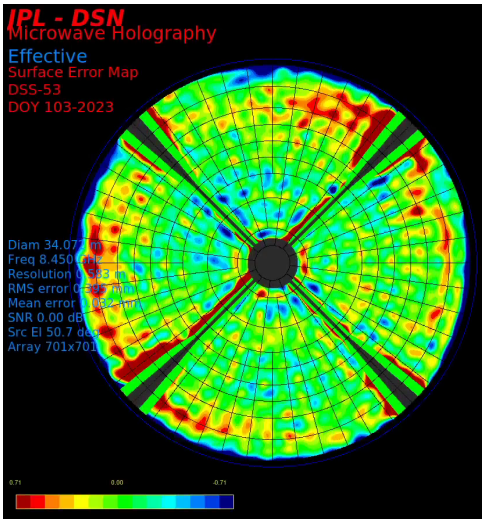

(b) Polar X-band 51 radius x 51 angles interpolated by 3

Figure 14. DSS-53 holographies close to rigging angle.

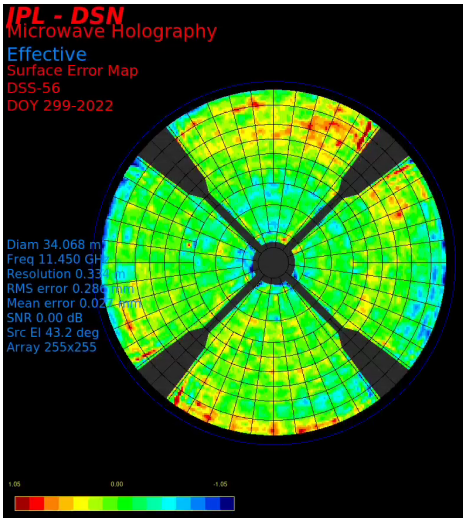

(a) Cartesian 127 x 127 Ku-band

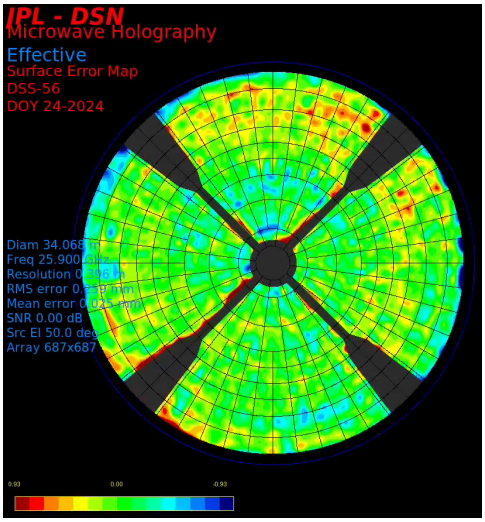

(b) Polar 75 x 75 K-band with JWST

Figure 15. DSS-56 high-resolution holographies.

IV. Conclusions

The adoption of polar sampling in CEI holography has been shown to significantly mitigate the impact of tropospheric turbulence on antenna surface measurements. By oversampling the boresight region and reducing motion artifacts, this approach enables reliable, all-weather holography, overcoming the limitations of traditional Cartesian grid methods. Although the processing complexity increases due to the fact that there is no exact solution for the inverse Fourier transform, the improved measurement repeatability and operational flexibility make polar sampling a powerful tool for DSN antenna diagnostics.

References

[1] A. Torre and M. Vazquez, "Connected-element interferometer holography via correlation of signals from the common platform," *The Interplanetary Network Progress Report*, vol. 42-241, Jet Propulsion Laboratory, Pasadena, California, pp. 1–19, May 2025.

[2] J. A. Fessler, *Image Reconstruction: Algorithms and Analysis*. University of Michigan, 2021.

[3] K. T. Block, "Advanced methods for radial data sampling in magnetic resonance imaging," tech. rep., Universitat Gottingen, 2008.

[4] S. Rasheed, M. Zakir, J. Tauqir, Z. Rasheed, and T. Ahmad, "Role of radial k space sampling technique in non-cooperative patients for the compensation of motion artifact in magnetic resonance imaging (MRI)," *The Professional Medical Journal*, vol. 29, no. 12, 2022.

[5] Y. Rahmat-Samii, "Surface diagnosis of large reflector antennas using microwave holographic metrology: An iterative approach," *Radio Science*, vol. 19, no. 5, pp. 1205–1217, Sept. 1984.

[6] M. L. Lauzon and B. K. Rutt, "Effects of polar sampling in k-space," *Magn Reson Med.*, vol. 36, no. 6, pp. 940–949, Dec. 1996.

[7] B. E. Coggins and P. Zhou, "Polar Fourier transforms of radially sampled NMR data," *Journal of Magnetic Resonance*, vol. 182, no. 1, pp. 84–95, 2006.

[8] R. J. Marks, *Advanced Topics in Shannon Sampling and Interpolation Theory*. New York, New York: Springer Verlag, 1993.

[9] S. A. Abbas, Q. Sun, and H. Foroosh, "An exact and fast computation of discrete Fourier transform for polar and spherical grid," *IEEE Transactions on Signal Processing*, vol. 65, pp. 2033–2048, Apr. 2017.

[10] S. A. Abbas, "2D 3D Polar Fourier Transform," 2017. GitHub. https://github.com/syedalamabbas/2D_3D_PolarFourierTransform.

[11] C. H. Lee, V. Vilnrotter, E. Satorius, Z. Ye, D. Fort, and K.-M. Cheung, "Large-array signal processing for deep-space applications," *The Interplanetary Network Progress Report*, vol. 42-150, Jet Propulsion Laboratory, Pasadena, California, pp. 1–28, Aug. 2002.